ANL-23/57

High-Energy X-ray Diffraction Microscopy for Nuclear Forensics FY23 Project Report

---

Strategic Security Sciences Division

About Argonne National Laboratory
Argonne is a U.S. Department of Energy laboratory managed by UChicago Argonne, LLC under contract DE-AC02-06CH11357. The Laboratory's main facility is outside Chicago, at 9700 South Cass Avenue, Lemont, Illinois 60439. For information about Argonne and its pioneering science and technology programs, see www.anl.gov.

DOCUMENT AVAILABILITY

Online Access: U.S. Department of Energy (DOE) reports produced after 1991 and a growing number of pre-1991 documents are available free at OSTI.GOV (http://www.osti.gov/), a service of the US Dept. of Energy's Office of Scientific and Technical Information.

Reports not in digital format may be purchased by the public from the National Technical Information Service (NTIS):
U.S. Department of Commerce
National Technical Information
Service 5301 Shawnee Rd
Alexandria, VA 22312
www.ntis.gov
Phone: (800) 553-NTIS (6847) or (703) 605-6000
Fax: (703) 605-6900
Email: **orders@ntis.gov**

Reports not in digital format are available to DOE and DOE contractors from the Office of Scientific and Technical Information (OSTI):
U.S. Department of Energy
Office of Scientific and Technical Information
P.O. Box 62
Oak Ridge, TN 37831-0062
www.osti.gov
Phone: (865) 576-8401
Fax: (865) 576-5728
Email: **reports@osti.gov**

Disclaimer

This report was prepared as an account of work sponsored by an agency of the United States Government. Neither the United States Government nor any agency thereof, nor UChicago Argonne, LLC, nor any of their employees or officers, makes any warranty, express or implied, or assumes any legal liability or responsibility for the accuracy, completeness, or usefulness of any information, apparatus, product, or process disclosed, or represents that its use would not infringe privately owned rights. Reference herein to any specific commercial product, process, or service by trade name, trademark, manufacturer, or otherwise, does not necessarily constitute or imply its endorsement, recommendation, or favoring by the United States Government or any agency thereof. The views and opinions of document authors expressed herein do not necessarily state or reflect those of the United States Government or any agency thereof, Argonne National Laboratory, or UChicago Argonne, LLC.

ANL-23/57

High-Energy X-ray Diffraction Microscopy for Nuclear Forensics FY23 Project Report

---

Prepared by:

*Derek R. McLain, ‡Jonathan D. Almer, ‡Xiaoxu Guo, *Katherine C. Hepler, *Anthony J. Krzysko, †Peter A. Mouche, ‡Hemant Sharma, †Yifen Tsai

*Strategic Security Sciences Division, †Chemical and Fuel Cycle Technology Division, ‡X-ray Science Division

Argonne National Laboratory

9/27/2023

Table of Contents

Executive Summary

Morphological information on nuclear material has been identified using visible light and scanning electron microscopy. These identify qualitative differences in particle morphology. Three-dimensional imaging of materials through alternating scanning electron microscopy imaging and focused ion beam milling has also been used. Unfortunately, these techniques are time- and labor-intensive, with significant sample preparation required and lengthy analysis times. Further, the resulting 3D images are qualitative, require manual identification, and do not capture statistically-representative populations. High energy X-ray 3D imaging using a direct-beam or diffracted-beam (High-Energy Diffraction Microscopy) have been developed at the Advanced Photon Source and can produce quantitative information on grains (phase, location, etc.) and pores (size distribution, sphericity) in a material. These techniques require only minutes to characterize a sample volume and are non-destructive, thus suitable for a wide range of existing samples and for confirmatory analyses to be carried out using conventional microscopy techniques.

In this second year of the project, all uranium oxide samples were analyzed via scanning electron microscopy (SEM) and the synchrotron techniques known as high energy x-ray diffraction microscopy (HEDM) and micro-computed tomography (μ-CT). The SEM characterization from year one of the project was repeated after the samples had been coated with a thin layer of carbon to minimize charge buildup on the oxide samples. The same SEM instrument was used for both image acquisition campaigns no statistically relevant differences were observed between the coated and uncoated samples, though image acquisition was significantly faster after applying the carbon coating.

Samples were analyzed at the Advanced Photon Source at beamline 1-ID in November of 2022. AI/ML techniques to de-noise data coming out of 1-ID during the analyses was also developed during this time using previously gathered data. Though samples were more powdery than typical for HEDM, it was possible to map the occurrence of UO_3 and U_3O_8 using the diffraction peaks associated with the different crystal structures through the use of diffraction tomography (DT). The resulting data shows that amorphous UO_3 is no longer present after calcining at any temperature and that crystalline UO_3 forms at 600 °C and slowly diminishes as the calcination temperature rises. It is unclear if this phenomenon would also be true if the calcination at lower temperatures was carried out for longer periods. Though quantitation of the different phases in a single sample has not been achieved, we believe a path forward has been identified.

Introduction

High energy X-ray 3D imaging techniques using a direct-beam (µ-CT) or diffracted-beam (HEDM) have been developed at APS over the last two decades and can produce quantitative information on crystallographic grains (phase, position, orientation, shape, size and lattice spacings) as well as pores (size distribution, sphericity) constituting a polycrystalline material.[1] This rich set of multi-dimensional information provides microstructural features of potential use for identifying processing parameters and material origin.[2] Further, these techniques only require minutes to characterize a full sample volume (~mm^3) and are non-destructive, making them suitable for a wide range of existing samples and for confirmatory analyses to be carried out using conventional microscopy techniques like SEM imaging. Though sub-surface structural characterization could offer significantly more information about a sample than simple surface characterization, it has not been a priority for the nuclear forensics scientific community or the proliferation detection community because the methods are relatively new – and therefore relatively unproven to this field – and analysis of this complex data is both time- and labor-intensive.[3,4] This project seeks to demonstrate the reliability of these advanced x-ray techniques for the nuclear forensics community and develop AI/ML-based methods to rapidly process and evaluate the large amounts of data they generate.

Sample Synthesis

The samples synthesized in FY22 as described in reference [5] were used for analyses carried out in FY23 as well.

Conventional Analyses

Scanning electron microscopy was repeated on the same samples analyzed in the previous FY after coating them with C to reduce charge build-up during imaging. The same FEI Strata 400 SEM-FIB DualBeam system with a field emission gun (FEG) electron source was using for particle imaging. Carbon coating was carried out using an SPI-MODULE Carbon coater with carbon fibers. Coating was accomplished using two one-second 19.5 amp pulses. Images were captured on the SEM with an acceleration voltage of 10kV and probe current of 130 pA. Images were acquired using a Continuous Dynode Electron Multiplier (CDEM) detector. Analysis of the collected images was carried out using the Morphological Analysis for Material Attribution (MAMA) software tool developed at Los Alamos National Laboratory. An image that has been segmented using the MAMA software is shown in Figure 1, with segmented particles highlighted in blue.

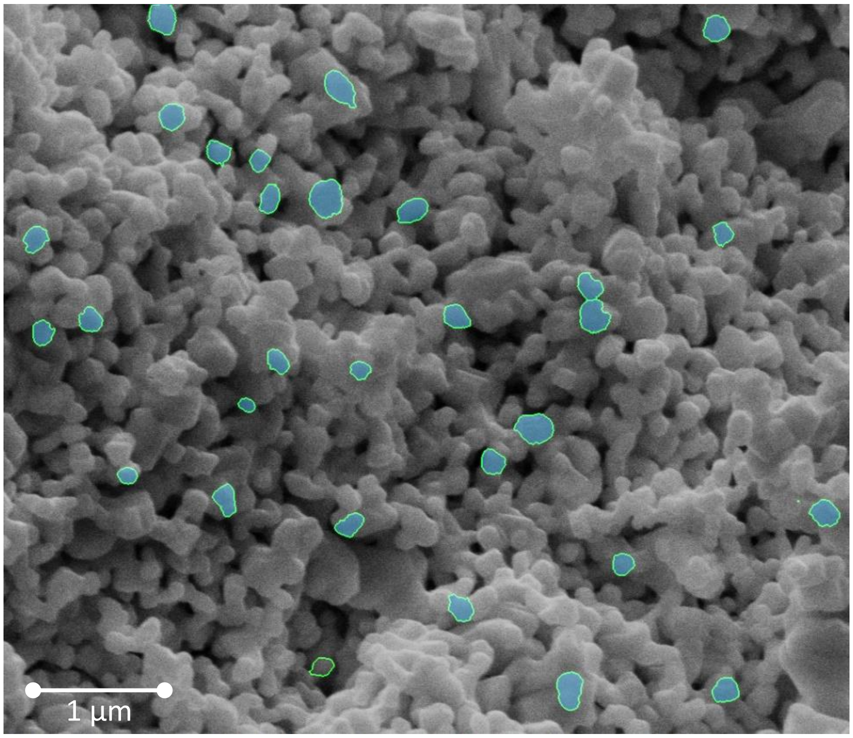

Figure 1:An SEM Image of U_3O_8 produced via calcination at 700°C that has been segmented using MAMA software.

The SEM image analysis was repeated because it was learned that the previous analyses published by *Olsen et al* also utilized thin coatings to dissipate charge buildup.[2] We therefore took this opportunity to compare analyses of uncoated and coated samples. The particle size distributions can be seen in Figure 2 for (a) uncoated and (b) carbon coated analyses. The particle size distribution broadened for each calcination temperature after coating, though this is very likely due to a larger number of particles being identified rather than a broadening of the individual particles. More particles were typically identified when analyzing the images of the coated samples because the images were of higher quality, owing better charge dissipation because of the carbon coating.

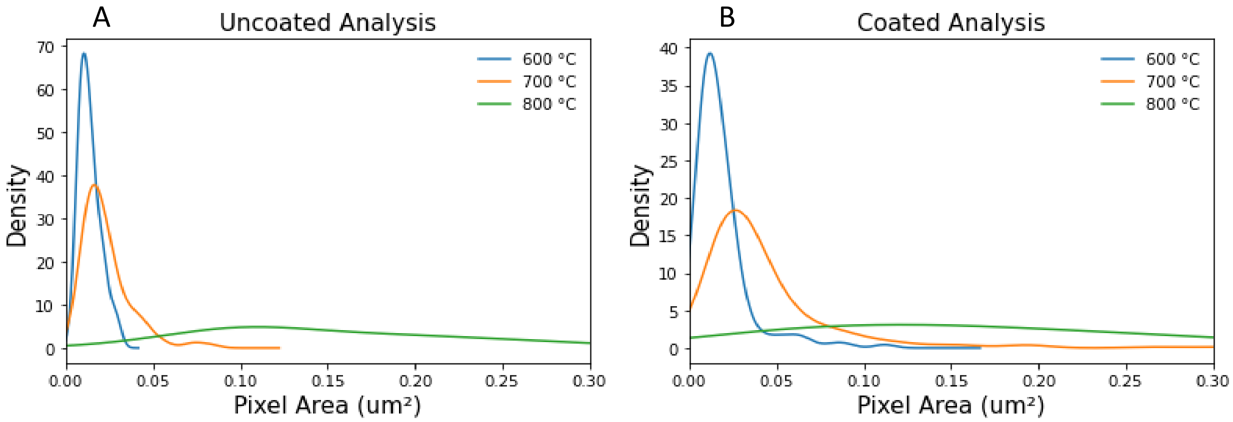

Figure 2: Particle distributions of (a) uncoated and (b) carbon coated SEM analyses of the same samples after calcination.

Despite using a maximum of 440 particles in our analysis, the trends we see of increased average particle size and broadening size distribution with increases in calcination temperature are similar to those seen by *Olsen et al [2]* and indicate that our prepared samples will be comparable to theirs.

Synchrotron Analysis

Sample Preparation

Synthesized solid samples were prepared for analysis at the APS in FY22. A description of preparation activities can be found in reference [5]. An image of one of the doubly encapsulated samples is seen below, in Figure 3.

Figure 3: Images of a) UO_3 packed in 0.5 mm diameter Kapton tubing, b) packed tubing mounted on a sample holder, and c) mounted sample with an additional layer of Kapton as secondary containment.

Data Collection

Though the full beamtime was not granted in FY22, the PI and Co-PIs worked together to get a short analysis scheduled between other users on an informal basis. The run took place in November of 2022. The ESAF review process was significantly simplified by using a sample containment that had previously been used for radioactive samples. The sample run itself was carried out at beamline 1-ID at the Advanced Photon Source (APS) and included both µ-CT and HEDM. Measurements were made using 90.5 keV incident photons focused to a roughly 2 µ m x 10 µ m beam size. Data collection took 1-2 hours for µ-CT of a complete sample. Due to the powdery nature of the samples, far-field (ff) HEDM and near field (nf) HEDM were not feasible, though diffraction tomography (DT), which utilizes a slightly different way of processing nf-HEDM measurements to interpret powder data, was possible. Effectively, the same signal is related to an individual voxel in DT, whereas the signal is related to a specific grain in HEDM.

However, each DT layer scan within a sample took roughly 2.5 hours. Due to the limited analysis time allotted, only 4-6 DT layer scans were completed for each sample. Also due to limited analysis time, only one sample of each type was characterized.

The experimental set-ups for µ-CT and HEDM are illustrated well by *Thomas et al* and *Schuren et al*, respectively, with the primary difference being how the x-ray data is collected and interpreted.[1,6] In this experiment, a single sample rotation rig was used for both techniques and the detector was changed to collect the different data. Figure 4 shows a photograph of one of the samples ready for analysis mounted on the rotational stage with the area detector for HEDM (in this case, DT) in the background and the µ -CT detector to the right of the image in the foreground.

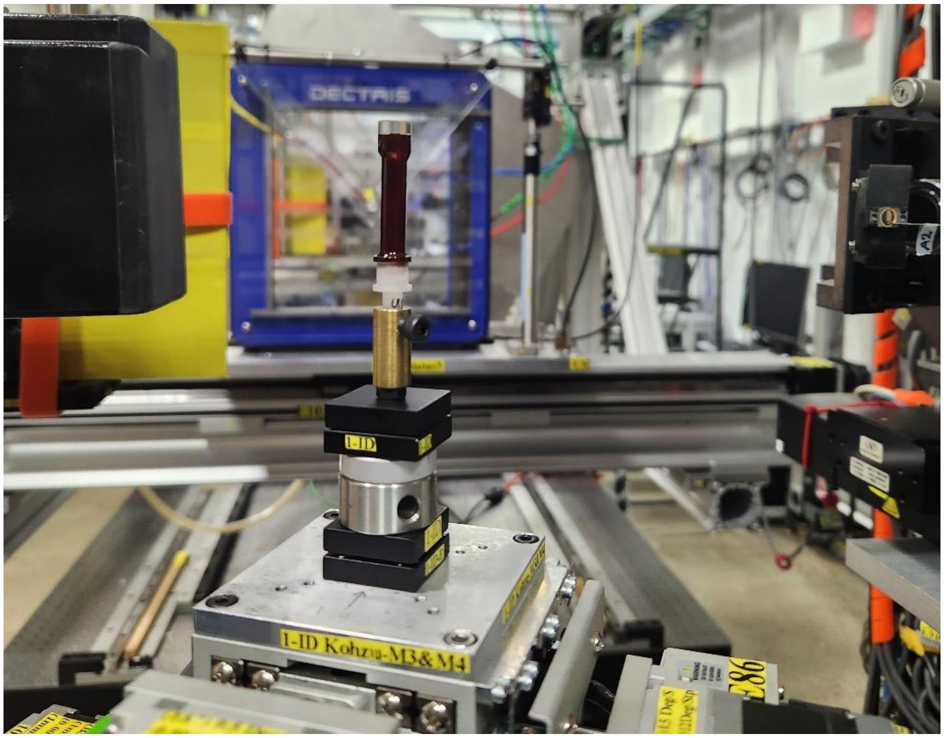

Figure 4: Sample mounted on the rotational stage at 1-ID, ready for analysis.

Reconstruction Techniques

The µ-CT data was reconstructed using the MIDAS suite [https://github.com/marinerhemant/midas.git]. After pre-processing the raw µ-CT images using custom Matlab routines developed at 1-ID, the reconstructions were processed on a local computer using 40 cores. We developed a custom algorithm for fast reconstruction of DT data. The algorithm includes a graphics user interface (using python and Tk) and a command-line interface (python) for setting up the reconstruction. Figure 5 is the designed workflow. Several things need to be noted:

1. The diffraction patterns are first integrated to extract one-dimensional information (Intensity vs. 2θ) shown in Figure 6. This step requires the user to select for both radius and azimuth, ranges and bins sizes. The algorithm applies necessary corrections to the detector images, then computes one integrated pattern for each frame and each chosen azimuth range.
2. The user then chooses a set of diifrraction peak positions for further analysis. For each of these peak positions, the algorithm will carry out tomography inversion using GridRec to compute the tomography reconstruction based on diffraction intensities.

This algorithm is highly optimized for reconstruction speed and RAM usage, it takes only ~5 minutes to run a full reconstruction from 160 GB of data on a local workstation.

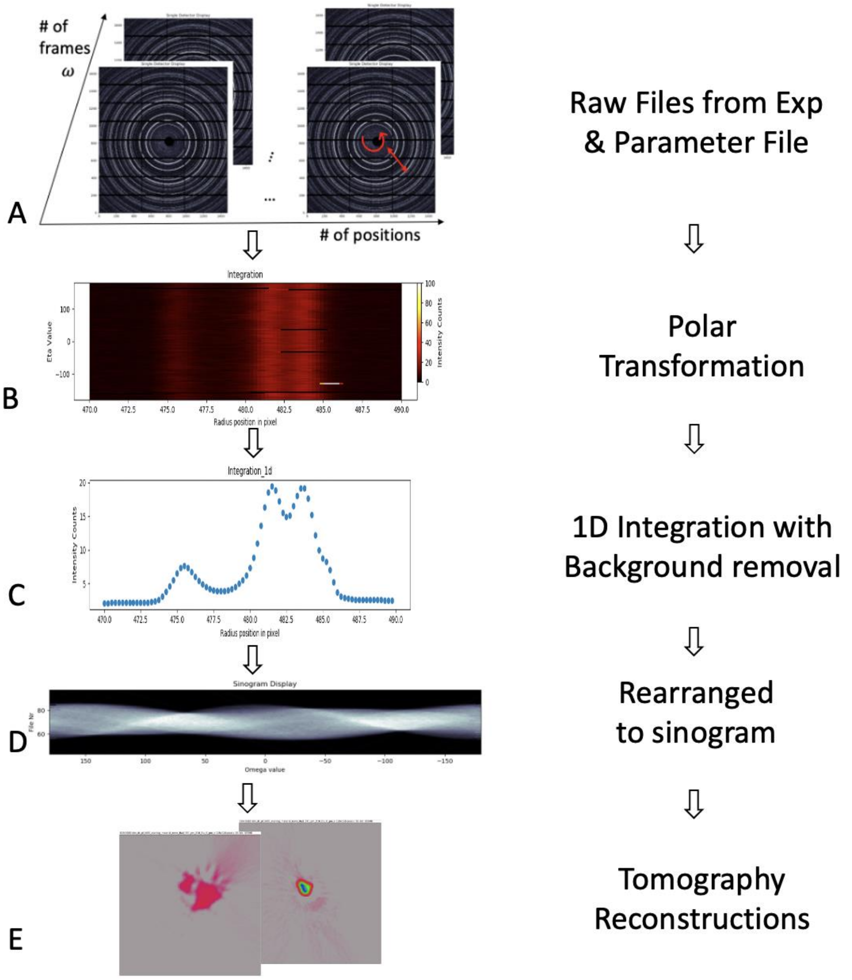

Figure 5: Diffraction tomography reconstruction workflow

Reconstructions

Reconstruction of the DT slices was carried out using different diffraction peaks corresponding to different U oxide compounds. Figure 6 shows the diffraction patterns of α-UO_3, $UO_3 \cdot 2H_2O$, and α-U_3O_8, and highlights the peaks used to identify these compounds in the DT slice reconstructions. An intense peak at 1.09° 2θ was used to identify $UO_3 \cdot 2H_2O$, while low-intensity peaks at 1.33° and 3.52° 2θ were used to identify α-U_3O_8. Two peaks were chosen in this case to ensure differentiation from α-UO_3, which has many peaks that overlap with α-U_3O_8 and could have been formed as an intermediate during calcination. Amorphous UO_3 (A-UO_3) was also mapped in reconstructions using diffraction intensity associated with 2.6° 2θ. This location does not correspond to any of the other crystal patterns and is in line with the location of a broad peak observed in the powder XRD (p-XRD) data collected in the previous fiscal year (not shown).

The presence of $UO_3 \cdot 2H_2O$ is likely a product of significant time elapsing between calcination and analysis, a large portion of which was outside of a controlled, low humidity atmosphere. While this was fortunate in that the crystalline UO_3 phase was easy to distinguish from the α-U_3O_8 using the 1.09° peak, it means that prompt analysis of a sample or *in-situ* analysis of a sample could be more difficult because of the overlapping nature of many α-U_3O_8 and α-UO_3 peaks. Generally, it seems these peaks overlap less as the 2θ angle increases. It is possible that the 5.5° peak at the edge of this plot would be effective, though further investigation and potentially even higher angle peaks would be better.

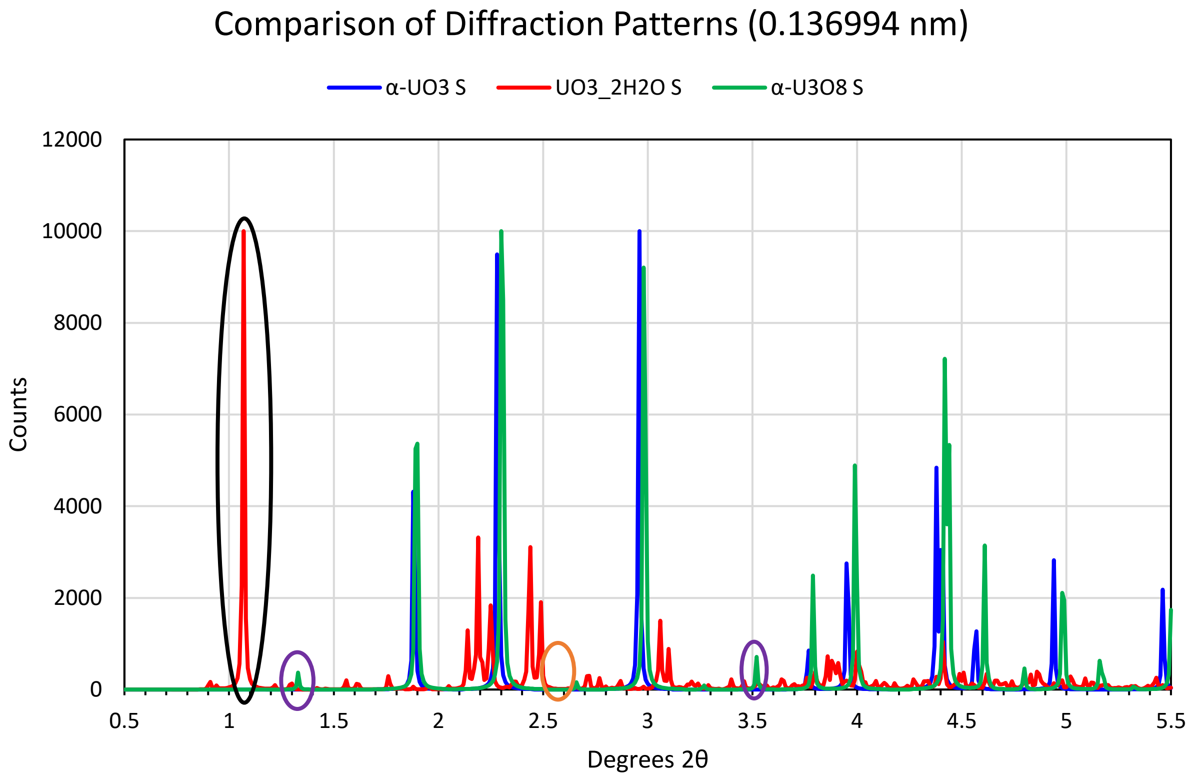

Figure 6: Plot of theoretical diffraction peaks for α-UO_3, $UO_3 \cdot 2H_2O$, and α-U_3O_8 as generated with an incident x-ray of wavelength 0.136994 nm (corresponding to beam energy used in experiments). Circles indicate peaks used to identify each crystal structure in reconstructions; black - $UO_3 \cdot 2H_2O$, orange - A-UO_3, purple - α-U_3O_8.

Reconstructed maps of the initial starting material are shown in Figure 7. It shows that even in the starting material there was a mixture of A-UO_3 and $UO_3 \cdot 2H_2O$, with the amorphous phase being found in larger grains and the hydrated crystalline phase found in smaller grains. There is also a single grain of α-U_3O_8 present in the sample, likely an artifact of using the same spatula while preparing multiple samples. The presence of all three expected crystal phases did offer the opportunity to test the efficacy of the peaks chosen for identification, and the exclusivity of the three phases identified indicates no meaningful overlap between them.

Subsequent reconstruction of slices from the samples calcined at 600 °C, 700 °C, and 800 °C (Figure 8, Figure 9, and Figure 10, respectively) show a rapid transition from A-UO_3 to $UO_3 \cdot 2H_2O$, with no discernable A-UO_3 signal even in the sample calcined at 600 °C. The signal present as a result of $UO_3 \cdot 2H_2O$ then gradually fades as calcination temperature increases, with no signal present in the 800 °C sample. Conversely, a gradual increase in signal intensity is observed for the peaks associated with α-U_3O_8, indicating that as calcination temperature increases the crystalline UO_3 phase is converted directly to α-U_3O_8.

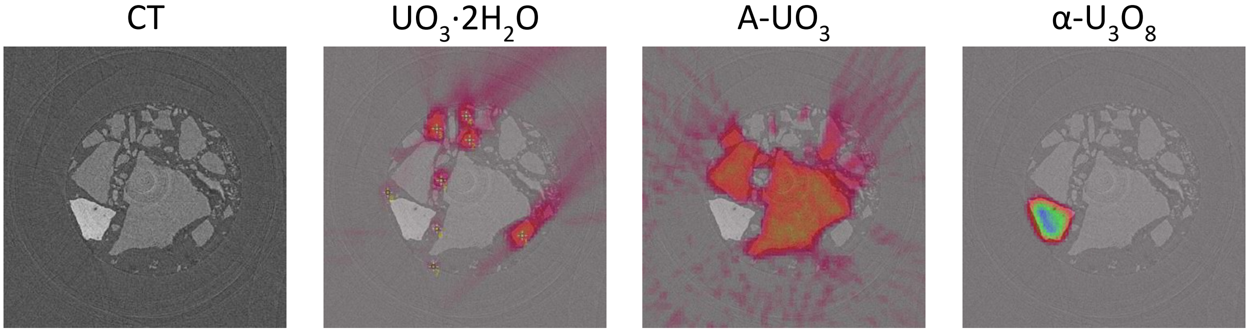

Figure 7: Reconstructed images from a single slice of UO_3 starting material. Images are (left) computed tomography, (mid-left) CT with $UO_3 \cdot 2H_2O$ intensity overlaid, (mid-right) CT with A-UO_3 intensity overlaid, and (right) CT with α-U_3O_8 intensity overlaid.

Overall, the calcined samples appear relatively uniform in composition. Each has a single bright spot that corresponds to Pt metal that is an artifact of scraping the Pt boat they were calcined in, but none have obvious heterogeneity within individual particles or between individual particles. Though these are very small subsamples of the material that was calcined, the overall homogeneity of them indicates a uniform transformation process and likely high uniformity in the temperature of the furnace.

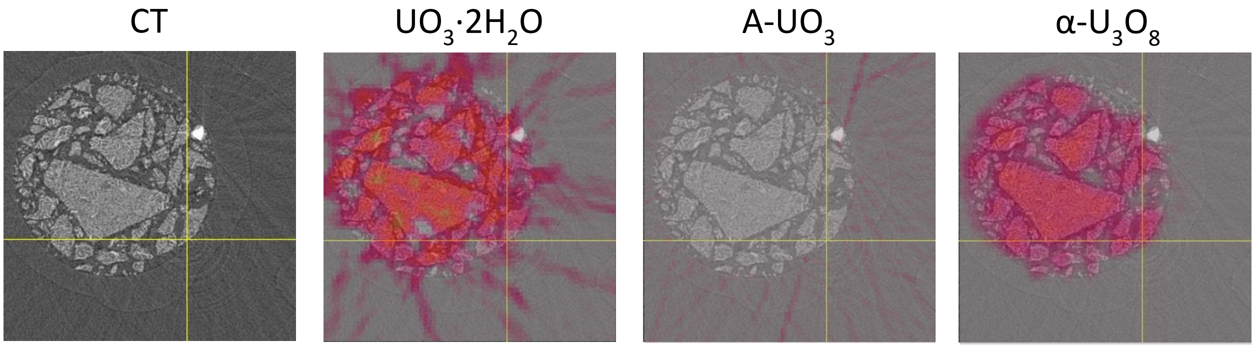

Figure 8: Reconstructed images from a single slice of material calcined at 600 °C. Images are (left) computed tomography, (mid-left) CT with $UO_3 \cdot 2H_2O$ intensity overlaid, (mid-right) CT with A-UO_3 intensity overlaid, and (right) CT with α-U_3O_8 intensity overlaid.

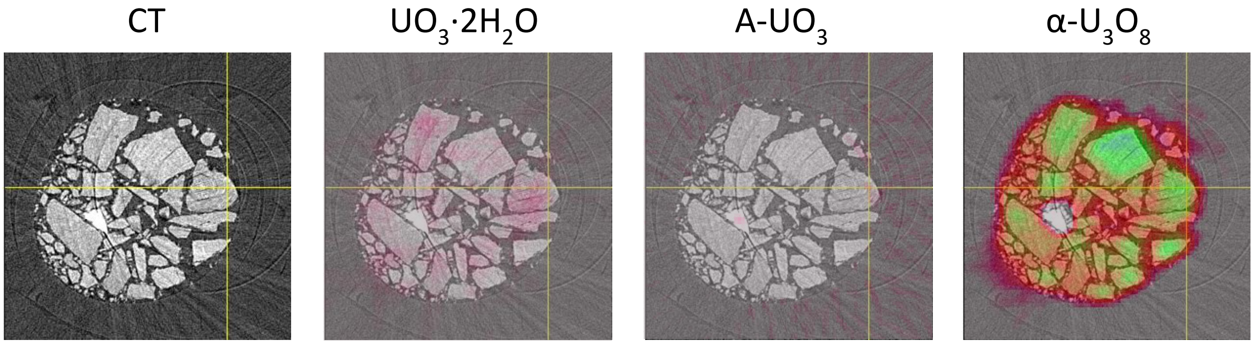

Figure 9: Reconstructed images from a single slice of material calcined at 700 °C. Images are (left) computed tomography, (mid-left) CT with $UO_3 \cdot 2H_2O$ intensity overlaid, (mid-right) CT with A-UO_3 intensity overlaid, and (right) CT with α-U_3O_8 intensity overlaid.

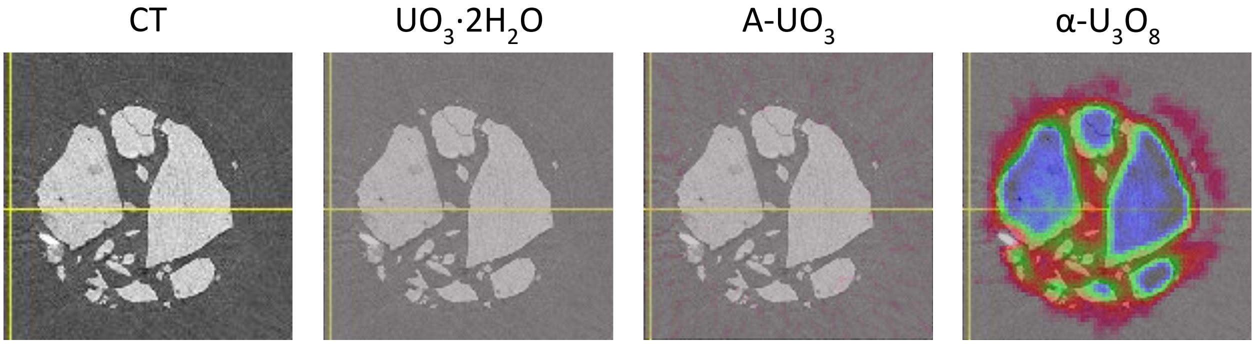

Figure 10: Reconstructed images from a single slice of material calcined at 800 °C. Images are (left) computed tomography, (mid-left) CT with $UO_3 \cdot 2H_2O$ intensity overlaid, (mid-right) CT with A-UO_3 intensity overlaid, and (right) CT with α-U_3O_8 intensity overlaid.

Summary

Four uranium oxide samples, prepared and characterized with conventional analytical chemistry techniques in the previous year, were analyzed at APS sector 1-ID using µ-CT and DT techniques. An advanced and highly optimized algorithm for reconstruction of DT data was developed. This algorithm takes only ca. 5 minutes to run a full reconstruction from 160 GB of data on a local workstation.

By reconstructing the intensities of various diffraction peaks associated with $UO_3 \cdot 2H_2O$, A-UO_3, and α-U_3O_8, it was possible to prepare distribution maps of the various crystal phases that resulted after calcination. These show the presence of small amounts of $UO_3 \cdot 2H_2O$ in the starting material, though the larger particles are all A-UO_3. All A-UO_3 signal is lost after calcination at 600 °C, indicating a relatively quick transition to a mixture of crystalline $UO_3 \cdot 2H_2O$ and α-U_3O_8. With increasing calcination temperature, the $UO_3 \cdot 2H_2O$ remaining after calcination steadily declines, with complete conversion to α-U_3O_8 after calcination at 800 °C. It is likely that the intermediate crystalline phase is not the hydrated UO_3 seen, but that α-UO_3 is formed in the furnace and hydrates to $UO_3 \cdot 2H_2O$ upon cooling and exposure to humid air. The observed homogeneity of the calcined particles indicates the process of converting from α-UO_3 to α-U_3O_8 is uniform in nature.

Future Work

Though this project is ending at the end of the FY, there are several avenues of investigation we would like to continue looking at. The first is to examine if the calcination time will play a part in the completeness of conversion, i.e. if a sample is calcined at 600 °C or 700 °C for a longer period, will the ratio of $UO_3 \cdot 2H_2O$ to α-U_3O_8 change? This will require several advancements, including the ability to discern the amount of each phase present based on the diffraction pattern peak intensity relationships. While it is common to estimate the amount of phase present in p-XRD samples using Rietveld refinement techniques, it is much rarer to do with DT data and, to our knowledge, has not been done with nuclear materials to date.[7-10]

Acknowledgement

This material is based upon work supported by Laboratory Directed Research and Development (LDRD) funding from Argonne National Laboratory, provided by the Director, Office of Science, of the U.S. Department of Energy under Contract No. DE-AC02-06CH11357.

References

1. Thomas J, Figueroa Bengoa A, Nori ST, Ren R, Kenesei P, Almer J, Hunter J, Harp J, Okuniewski MA (2020) The application of synchrotron micro-computed tomography to characterize the three-dimensional microstructure in irradiated nuclear fuel. *J Nucl Mater* **537** p. 152161. doi:https://doi.org/10.1016/j.jnucmat.2020.152161
2. Olsen AM, Richards B, Schwerdt I, Heffernan S, Lusk R, Smith B, Jurrus E, Ruggiero C, McDonald LW (2017) Quantifying Morphological Features of α-U3O8 with Image Analysis for Nuclear Forensics. *Anal Chem* **89**:5 p. 3177-3183. doi:10.1021/acs.analchem.6b05020
3. Donald SB, Chung BW (2022) Morphological and chemical characteristics of oxide scales formed on δ-phase plutonium metal alloys II: 2.0 at% Ga. *J Nucl Mater* **559** p. 153473. doi:https://doi.org/10.1016/j.jnucmat.2021.153473
4. Lewis SR, Simonetti A, Corcoran L, Spano TL, Chung BW, Teslich NE, Burns PC (2018) Characterization of uraninite using a FIB–SEM approach and its implications for LA–ICP–MS analyses. *J Radioanal Nucl Chem* **318**:2 p. 1389-1400. doi:10.1007/s10967-018-6232-3
5. McLain DR, Almer JD, DeAngeles KJ, Guo X, Hepler KC, Krzysko AJ, Laudadio ED, Mouche PA, Sharma H, Tsai Y (2022) High-Energy X-ray Diffraction Microscopy for Nuclear Forensics FY2022 Project Report. Argonne National Laboratory, United States. doi:10.2172/1893314
6. Schuren JC, Shade PA, Bernier JV, Li SF, Blank B, Lind J, Kenesei P, Lienert U, Suter RM, Turner TJ, Dimiduk DM, Almer J (2015) New opportunities for quantitative tracking of polycrystal responses in three dimensions. *Curr Opin Solid State Mater Sci* **19**:4 p. 235-244. doi:https://doi.org/10.1016/j.cossms.2014.11.003
7. Frolich S, Leemreize H, Jakus A, Xiao X, Shah R, Birkedal H, Almer JD, Stock SR (2016) Diffraction tomography and Rietveld refinement of a hydroxyapatite bone phantom. *J Appl Crystallogr* **49**:1 p. 103-109. doi:doi:10.1107/S1600576715022633
8. Palle J, Wittig NK, Kubec A, Niese S, Rosenthal M, Burghammer M, Grünewald TA, Birkedal H (2020) Nanobeam X-ray fluorescence and diffraction computed tomography on human bone with a resolution better than 120 nm. *Journal of Structural Biology* **212**:3 p. 107631. doi:https://doi.org/10.1016/j.jsb.2020.107631
9. Stock SR, Park JS, Jakus A, Birkbak M, Frølich S, Birkedal H, Shah R, Almer JD (2021) In situ loading and x-ray diffraction quantification of strains in hydroxyapatite particles within a 3D printed scaffold. *Materialia* **18** p. 101174. doi:https://doi.org/10.1016/j.mtla.2021.101174
10. Birkbak ME, Nielsen IG, Frolich S, Stock SR, Kenesei P, Almer JD, Birkedal H (2017) Concurrent determination of nanocrystal shape and amorphous phases in complex materials by diffraction scattering computed tomography. *J Appl Crystallogr* **50**:1 p. 192-197. doi:doi:10.1107/S1600576716019543

ANL-23/57

Strategic Security Sciences Division
Argonne National Laboratory
9700 South Cass Avenue, Bldg. 205
Lemont, IL 60439

www.anl.gov